



## Quantifying the single scattering albedo for the January 2017 Chile wildfires from simulations of the OMI absorbing aerosol index

Jiyunting Sun<sup>1,2</sup>, J. Pepijn Veefkind<sup>1,2</sup>, Peter van Velthoven<sup>1</sup>, Pieternel F. Levelt<sup>1,2</sup>

<sup>1</sup>Royal Netherlands Meteorological Institute, De Bilt, 3731 GA, the Netherlands

<sup>2</sup>Department of Geoscience and Remote Sensing (GRS), Civil Engineering and Geosciences, Delft University of Technology, Delft, 2628 CD, the Netherlands

Correspondence to: Jiyunting Sun ([jiyunting.sun@knmi.nl](mailto:jiyunting.sun@knmi.nl))

**Abstract.** The absorbing aerosol index (AAI) based on the near Ultra-Violet (near-UV) remote sensing techniques is a qualitative parameter that allows to retrieve aerosol optical properties with confidence. In the first part of this study, a series of AAI sensitivity analysis is presented exclusively on biomass burning aerosols. Later on, this study applies a radiative transfer model (DISAMAR) to simulate the AAI measured by the Ozone Monitoring Instrument (OMI) and to derive the aerosol single scattering albedo ( $\omega_0$ ). The inputs for the radiative transfer calculations are satellite measurement geometry and surface conditions from OMI, aerosol optical thickness ( $\tau$ ) from the MODerate-resolution Imaging Spectroradiometer (MODIS), and aerosol micro-physical parameters from the AERosol RObotic NETwork (AERONET), respectively. This approach is applied to the Chile wildfires for the period from 26 to 30 January 2017, when the OMI observed AAI of this event reached its peak. The Cloud and Aerosol Lidar with Orthogonal Polarization (CALIOP) failed to capture the evolution of the smoke plume, therefore the aerosol profile is parameterized. The simulated plume ascends to an altitude of 4.5–4.9 km, which is in good agreement with measurements. Due to the relatively small data size of this case, an outlier detection criterion has to be applied. The results show that the AAI simulated by DISAMAR is consistent with observations. The correlation coefficients are over 0.85. The retrieved mean  $\omega_0$  at 550 nm is approximately 0.84, slightly smaller than the value of 0.90 measured independently by the AERONET instrument. The relative distance between the AERONET site and the plume, the assumption of homogeneous and static plume properties, the lack of the aerosol profile information, and the uncertainties in observations are primarily responsible for this discrepancy. Except for the observational errors, the impact of remaining error sources on  $\omega_0$  retrieval is difficult to quantify.

### 25 1 Introduction

Biomass burning aerosols are generated from combustion of carbon-containing fuels, either by natural or anthropogenic processes (Bond et al., 2004; IPCC, 2014). They consist of fine particles (aerodynamic diameter smaller than 2.5  $\mu\text{m}$ ) that have adverse impacts on the environment and human health (Bäumer et al., 2008; Adler et al., 2011). Biomass burning aerosols are also of great concern from the perspective of climate. They contain absorbing aerosols, which exert a positive radiative forcing to the climate. According to the latest Intergovernmental Panel on Climate Change (IPCC) report (IPCC, 2014), one type of absorbing aerosol, black carbon (BC), can be considered as the second important warming agent after carbon dioxide. Absorbing aerosols heat the atmosphere primarily by interaction with solar radiation. They directly absorb the incoming or reflected sunlight. They are also able to reduce the reflectivity of the planet by depositing on bright surfaces (Huang et al., 2013) or by enhancing the absorption of clouds (Kaufman and Boucher, 2002; Ramanathan and Carmichael, 2008; Bond et al., 2013). Besides, the heating by absorbing aerosols changes the atmospheric thermal structure and surface energy budget that may further perturb cloud distribution, the so-called semi-direct effect (IPCC, 2007; Koch and Del Genio, 2010).

Quantifying the climate effect of absorbing aerosols is therefore important. The reported radiative forcing of BC produced by fossil fuel and biofuel is around 0.4  $\text{Wm}^{-2}$  (0.05 – 0.80  $\text{Wm}^{-2}$ ) (Ramanathan and Carmichael, 2008; Bond et al., 2013; Huang



40 et al., 2013). But this estimate is highly uncertain. Accurate measurements of the aerosol single scattering albedo ( $\omega_0$ ) on a  
global scale can reduce the uncertainty in radiative forcing assessments (Hu et al., 2007).  $\omega_0$  is defined as the ratio of the  
radiation scattered by aerosol particles to the total attenuation. Because aerosol compositions and properties are highly  
variable in space and time, measuring the global distribution of  $\omega_0$  relies on remote sensing techniques. The POLarization  
and Directionality of the Earth's Reflectances (POLDER) measures aerosol polarized phase function. This provides  
45 information directly related to  $\omega_0$  (Leroy et al., 1997). But there is no continuous temporal coverage because the first two  
instruments encountered technical hitches that prematurely ended the missions. As a result,  $\omega_0$  is usually retrieved by forward  
simulations that are adapted to observational parameters. Many implementations have been done for ground-based network  
measurements (Dubovik et al., 1998; Eck et al., 2003; Petters et al., 2003; Kassianov et al., 2005; Corr et al., 2009; Yin et al.,  
2015), while relatively fewer applications to satellite instruments exist due to lack of validation (Lee et al., 2007; Ialongo et  
50 al., 2010; Eck et al., 2013). Moreover, a majority of those methods heavily depend on the aerosol optical thickness ( $\tau$ ), either  
in forward model simulations or in validation procedures. This makes the derived  $\omega_0$  subject to large uncertainties. The  
reason is that  $\tau$  retrieval requires assumptions on aerosol types, and the commonly used  $\tau$  that is retrieved in the visible band  
where the signal of bright surfaces is strong. Besides, the aerosol effect on radiance is inversely proportional to wavelength  
(Kaufman, 1993), and the sensitivity to  $\omega_0$  is not significant for most  $\tau$  measurements in the visible and infrared band  
55 (Kaufman et al., 1997).

The near Ultra-Violet (UV) instruments provide an improved methodology that constrains forward model simulations with  
the absorbing aerosol index (AAI) (Herman et al., 1997). The near-UV AAI is a qualitative measure of absorbing aerosols  
that was first provided by the Total Ozone Mapping Spectrometer (TOMS) on-board Nimbus-7 in 1979. Since then several  
instruments have contributed to the AAI data record, that now spans more than 35 years. This long data record is an  
60 important motivation for improving methods to derive quantitative aerosol information from the near-UV.

The foremost advantage of the AAI is its independence from assumptions on aerosol types, which significantly reduce the  
retrieval uncertainty. Ginoux et al. (2004) suggested that comparing model simulations with AAI from TOMS allows a better  
control of discrepancies because the only error source is the model. Further advantages of the near-UV channel are the low  
reflectivity of the Earth's surface and the absence of significant molecular absorption. Using this band can ensure the aerosol  
65 absorption is one of the major contributors to the total signal. Moreover, the sensitivity of  $\tau$  in the visible band to  $\omega_0$  is lower  
over dark surfaces (Kaufman et al., 1997), while the near-UV AAI is by definition highly sensitive to  $\omega_0$ . Previous studies  
have proven the potential of the near-UV AAI from TOMS in aerosol properties retrieval. Torres et al. (1998) provided the  
theoretical basis of an inversion method to derive  $\tau$  and  $\omega_0$  from backscattered radiation. This method was validated by  
ground-based observations during the Southern African Regional Science Initiative (SAFARI) 2000 measurement campaign.  
70 The agreement of  $\tau$  and  $\omega_0$  reaches  $\pm 30\%$  and  $\pm 0.03$ , respectively (Torres et al., 2005). Hu et al. (2007) retrieved global  
columnar  $\omega_0$  based on the AAI from TOMS with an average uncertainty of 15%.

Empirical models were also developed to build connections between the AAI and parameters it depends on. Hsu et al. (1999)  
found a linear relation between the TOMS retrieved AAI and Sun-photometer measured  $\tau$  over regions with biomass burning  
and regions covered by African dust. Ginoux and Torres (2003) implemented an empirical relation between the AAI  
75 retrieved from TOMS with  $\tau$ ,  $\omega_0$  and surface pressure ( $P_s$ ) to characterize the dust aerosols. Although requiring less  
computational cost, applying these empirical models is either limited by specific conditions or subject to large errors. Thus,  
these methods have not been widely used.

This study follows previous research, that uses the near-UV AAI provided by the Ozone Monitoring Instrument (OMI) on-  
board Aura, the successor of TOMS, to derive the aerosol properties of the Chile wildfires in January 2017. Triggered by a  
80 combination of long-term drought and high temperature, this series of fires occurring in central Chile (Pichilemu 34.39°S  
72.00°W and Constitución 35.33°S, 72.42°W) was regarded as the worst wildfire season in the national history (The  
Guardian, 2017). The fires led to evacuations of the affected areas, and caused massive losses of the local forestry industry



(pine and eucalyptus forests) (NASA. gov, 2017). The smoke plume was transported away from the source regions towards the tropical area in the Pacific Ocean by north-westward winds (Fig.1). In this study, we quantitatively retrieve the  $\omega_0$  of this smoke by simulating the near-UV AAI from OMI with the radiative transfer model Determining Instrument Specifications and Analysing Methods for Atmospheric Retrieval (DISAMAR). The aerosol inputs of DISAMAR includes the  $\tau$  retrieved from the MODerate-resolution Imaging Spectroradiometer (MODIS) on-board the NASA EOS Aqua satellite, and information on aerosol micro-physical parameters provided by AERONET. In the next section, we provide a brief introduction on the near-UV AAI and its sensitivity to various parameters. The retrieval methodology is described in section 3. In section 4, retrieved results and uncertainty analysis of Chile 2017 wildfires are discussed, followed by main conclusions in section 5.

## 2 AAI sensitivity studies based on DISAMAR

In this section, we first introduce the near-UV AAI. In the sensitivity analysis, we show that the AAI depends not only on aerosol parameters, but also on the surface conditions and the observation geometry. The sensitivity analysis in this study is only designed for biomass burning aerosols.

### 2.1 Near-UV AAI definition

The concept of the near-UV AAI was first conceived to detect UV-absorbing aerosols from the spectral contrast provided by TOMS observations, known as the residue method (Herman et al., 1997). The basic idea of the residue method is that for a pure Rayleigh atmosphere, where the reflectance, or equivalently the radiance ( $I_\lambda$ ), decreases strongly with the wavelength. The presence of absorbing aerosols will reduce this spectral dependency of  $I_\lambda$ . The change in this wavelength dependency is summarized as the AAI, which is calculated from the  $I_\lambda$  at the wavelength pair  $\lambda_1$  and  $\lambda_2$ :

$$AAI = -100 \left( \log_{10} \left( \frac{I_{\lambda_1}}{I_{\lambda_2}} \right)^{obs} - \log_{10} \left( \frac{I_{\lambda_1}}{I_{\lambda_2}} \right)^{Ray} \right), \quad (1)$$

The *obs* and *Ray* denote the satellite observed and the model calculated  $I_\lambda$ , respectively. The longer wavelength  $\lambda_2$  is treated as reference wavelength where the surface albedo ( $a_s$ ) is determined by fitting the observed radiance. This  $a_s$  is also assumed at  $\lambda_1$  to compute  $I_{\lambda_1}^{Ray}$ . Consequently, Eq.(1) can be equivalently transformed into the difference between  $I_{\lambda_1}^{obs}$  and  $I_{\lambda_1}^{Ray}$  normalized by the measured radiance  $I_{\lambda_1}^{obs}$ :

$$AAI = 100 \log_{10} \left( \frac{\Delta I_{\lambda_1}}{I_{\lambda_1}^{obs}} + 1 \right) \quad (2)$$

### 2.2 Near-UV AAI sensitivity studies

The sensitivity studies are performed with the radiative transfer model DISAMAR. It simulates the forward  $I_\lambda$  spectrum and retrieves the atmospheric or surface properties. The wide spectral coverage (0.27–2.4  $\mu\text{m}$ ) ensures that it is capable to retrieve various atmospheric components (trace gases, aerosols, clouds, etc.) and surface conditions for passive remote sensing (De Haan, 2011). DISAMAR uses either the Doubling-Adding method or the Layer Based Orders of Scattering (LABOS) for radiative transfer calculations. This study uses the latter one because it is less computationally intensive (De Haan et al., 1987; De Haan, 2011).

DISAMAR allows to apply several aerosol scattering approximations. Here we assume Mie scattering aerosols. Given size distribution function ( $r_g$ ), complex refractive index ( $n_r$  and  $n_i$ ) at specific wavelengths and a certain wavelength interpolation method, DISAMAR calculates the spectrally dependent optical properties (e.g.  $\omega_0$  and phase function  $P(\Theta)$ ) within the specified wavelength range. In this study, we use the linear interpolation and the spectrum coverage from 340 to 675 nm. The parameters to describe Mie particles and their corresponding values are listed in Table 1. Considering the Chile wildfires



120 that mainly produced biomass burning aerosols, these sensitivity studies are specifically performed for parameterized smoke aerosols with only fine mode particles and weak linearly wavelength dependency in  $n_r$  and  $n_i$ . The default values refer to observations of the daily average of the AERONET station Santiago Beauchef (33.46°S, 70.66°W) and the corresponding  $P(\Theta)$  at 354 nm is presented in Fig.2. DISAMAR requires  $\tau$  should be defined at 550 nm. Surface influences include spectrally flat  $a_s$  and  $P_s$ . The aerosol profile is parameterized as a single layer box shape, with its bottom at  $z_{\text{aer}} - \Delta z/2$  and top at  $z_{\text{aer}} + \Delta z/2$ , where  $z_{\text{aer}}$  and  $\Delta z$  are the geometric central height and the geometric thickness of the aerosol layer, respectively. The whole sensitivity analysis is performed for cloud-free conditions. The wavelength pair of OMI (354 and 388 nm) is applied to compute the AAI. To make it comparable, the AAI calculated in this section is normalized by the maximum value among each sensitivity study. Note that each sensitivity study always uses the default settings listed in Table 1 unless different values are explicitly mentioned.

130 Aerosol optical properties are determined by micro-physics, such as the real and imaginary part of complex refractive index ( $n_r$  and  $n_i$ ), and the particle size ( $r_g$ ). The effect of the complex refractive index is dual. As shown in Fig.3 (a), an increase in the real refractive index  $n_r$  directly enhances the magnitude of  $I_{\lambda 1}^{\text{obs}}$ , whereas  $\Delta I_{\lambda 1}$  reduces. This results in low values of the AAI, which correspond to a large  $\omega_0$  (Fig.3 (b)). The asymmetry factor  $g$  is the averaged cosine of the scattering angle  $\Theta$ , weighted by  $P(\Theta)$ . Under condition that measurement geometry is  $\Theta = 150^\circ$ , the declining  $g$  implies that more light is scattered in the line-of-sight of the detector, thus the higher  $I_{\lambda 1}^{\text{obs}}$ . Conversely, the imaginary refractive index  $n_i$ , which is directly associated with  $\omega_0$ , has an opposite influence (Fig.3 (c) and (d)).

The particle size distribution has a more complicated influence on the AAI. As shown in Fig.3 (e) and (f), even with a decreasing  $\omega_0$  and an increasing  $g$ , or alternatively a decreasing  $I_{\lambda 1}^{\text{obs}}$ , the AAI primarily follows the behaviour of  $\Delta I_{\lambda 1}$ . The significant reduction in the spectral dependency of  $I_\lambda$  overwhelms the high reflectivity for small particles ( $r_g = 0.1 \mu\text{m}$ ).

140 The concentration and vertical distribution of aerosols also have a strong influence on the wavelength dependency of the radiance  $\Delta I_{\lambda 1}$ . As shown in Fig.4 (a), the AAI is positively correlated with  $\tau$  as its definition (Eq.(1)). The AAI is highly sensitive to the aerosol vertical distribution (Herman et al., 1997; Torres et al., 1998; de Graaf et al., 2005). As the aerosol layer ascends (Fig.4 (b)), more molecular scattering beneath the aerosol layer is shielded, which reduces  $I_{\lambda 1}^{\text{obs}}$  while it increases  $\Delta I_{\lambda 1}$ . The relation between the AAI and  $z_{\text{aer}}$  is almost linear. Fig.4 (c) shows that at the same altitude, the AAI slightly increases with the geometrical thickness of an aerosol layer. The possible reason could be that a larger  $\Delta z$  indicates a longer light path through the absorbing layer, amplifying the absorption of the aerosol layer.

150 The calculated AAI does not only depend on the aerosols themselves, but also on ambient parameters such as surface and clouds. Although the near-UV AAI is capable to distinguish absorbing and non-absorbing agents (Herman et al., 1997), even retrieve aerosol information over clouds (Torres et al., 2012), the uncertainty triggered by clouds is relatively high and therefore the cloudy conditions are not included in this study. Surface conditions are generally parameterized by  $P_s$  and  $a_s$ . It can be seen in Fig.5 (a) that a decline in  $P_s$ , or equivalently an elevated terrain height, leads to less Rayleigh scattering shielded between the surface and the aerosol layer. As a result, the AAI decreases significantly due to smaller  $\Delta I_{\lambda 1}$ . This is in agreement with a previous study (de Graaf et al., 2005), where it was found that the retrieved AAI could be highly overestimated without correction for terrain height. According to de Graaf et al. (2005), increasing  $a_s$  has two counteracting effects. On the one hand, it increases the amount of directly reflected radiation at the top of the atmosphere, namely a larger  $I_{\lambda 1}^{\text{obs}}$ , on the other hand it enhances the role of absorption by the aerosol layer rather than the surface, namely a larger  $\Delta I_{\lambda 1}$ . Which effect of  $a_s$  is decisive depends on  $P_s$  (Fig.5 (b)). When the aerosol layer is relative to the sea level ( $P_s = 1013 \text{ hPa}$ ), the first effect dominates. However, a brighter surface compensates the loss of molecular scattering shielded by the aerosols when the terrain height rises ( $P_s = 813 \text{ hPa}$ ), which makes the absorbing layer more detectable.

160 The AAI depends also on the Sun-satellite geometry. Here we provide the AAI as a function of the measurement geometries for the default case with the relative azimuth angle  $\Delta\phi = 180^\circ$ . As presented in Fig.6 (a), the AAI becomes very sensitive to the geometries for zenith angles larger than  $60^\circ$ , which confirms previous research (Herman et al., 1997; Torres et al., 1998;



de Graaf et al., 2005). This is mainly due to the significant growth of  $P(\Theta)$  when  $\Theta$  becomes smaller (Fig.2). It is thus suggested that the OMI measurement with  $\theta_0$  larger than this value should be removed due to large variations in the AAI. To  
165 analyse the radiance behaviour as previously, we plotted the  $I_{\lambda_1}^{obs}$  and  $\Delta I_{\lambda_1}$  as functions of  $\Theta$  along the cross section, respectively (Fig.6 (b)). It is noted that  $I_{\lambda_1}^{obs}$  corresponding to the selected  $\Theta$  does not strictly follow the changes in  $P(\Theta)$  (Fig.2). This could be the reason that the length of the light path through the aerosol layer also varies with the measurement geometry. Although the overall change in  $P(\Theta)$  with an increasing  $\Theta$  is negative, the light path within the aerosol layer also decreases. Less absorption occurring in the aerosol layer overwhelms the decrease in reflectivity for larger  $\Theta$ , resulting in an  
170 increase in  $I_{\lambda_1}^{obs}$  with  $\Theta$ .

### 3 Methodology and datasets

In this section, we first present the datasets involved and their pre-processing, followed by the strategy to retrieve the aerosol  $\omega_0$  with additional constraint of the near-UV AAI from OMI. Although the DISAMAR can calculate wavelength dependent,  $\omega_0$  at 550 nm is used as retrieved value for the consistent comparison with AERONET measurements.

#### 175 3.1 Datasets

##### 3.1.1 OMI and GOME-2 absorbing aerosol index

The TOMS near-UV AAI retrieval has been proven a robust algorithm and applied to successive sensors, such as OMI on-board Aura and GOME-2 on-board MetOp-A/B. GOME-2 has higher spectral resolution (0.2-0.4 nm) than TOMS, but the spatial resolution is rather coarse ( $40 \times 40 \text{ km}^2$ ). In this study, GOME-2 measured AAI at wavelength pair 340 and 380 nm is  
180 only used as an independent dataset to assess the potential bias of the OMI measurements.

OMI combines advantages of both TOMS and GOME-2. It covers wavelengths from 264 to 504 nm with a spectral resolution of approximately 0.5 nm and has a much higher spatial resolution than GOME-2 of  $13 \times 24 \text{ km}^2$  (Levelt et al., 2006). Since OMI was launched in 2004, the AAI retrieved from this instrument has been widely used in various applications. Kaskaoutis et al. (2010) employed the OMI measured AAI for regional research of the aerosol temporal and  
185 spatial distribution in Greece. Torres et al. (2012) utilized the advantage of near-UV AAI to detect aerosols over clouds. The OMI observed AAI was even used to evaluate the impact of surface dust loading on human health (Deroubaix et al., 2013). Buchar et al. (2015) validated the NASA MERRA aerosol reanalysis with the AAI retrieved from OMI.

In this study, the OMI level 2 product OMAERO is used to provide AAI retrieved by the wavelength pair of 354 and 388 nm, and the corresponding measurement geometry and the surface conditions. The samples are included in the radiative transfer simulation only if  $\theta_0$  are smaller than  $60^\circ$ , and if ground pixels are not contaminated by sun-glint, clouds, row anomalies of the instrument, etc. The simulation is only applied to plume pixels, which are defined for both OMI and GOME-2 retrieved AAI values larger than 1.

##### 3.1.2 MODIS, OMI and AERONET aerosol optical thickness

MODIS on-board Aqua/Terra is a sensor that was specifically designed for atmosphere and climate research. The  
195 combination of two satellites ensures a global coverage per 1 to 2 days. The spatial resolution can reach 1 km and the spectrum ranges from 0.4 to  $14.4 \mu\text{m}$  (Remer et al., 2005). MODIS employs separated algorithms for aerosol retrieval over oceans and land, respectively (Tanré et al., 1997; Kaufman and Tanré, 1998; Hsu et al., 2004; Remer et al., 2005). Currently the  $\tau$  provided by MODIS is one of the most reliable datasets (Lee et al., 2009), with an estimated uncertainty of only 3-5% over ocean and 5-15% over land (Remer et al., 2005). As mentioned before, DISAMAR requires  $\tau$  at 550 nm. This study  
200 uses cloud-filtered  $\tau$  at 550 nm from the level 2 product MYD04 as the input for radiative transfer calculation.



In addition, the  $\tau$  measured by OMI and AERONET are treated as a reference dataset to evaluate potential biases in MODIS. The OMAERO retrieval uses multi-spectral fitting techniques. The retrieved  $\tau$  is in good accordance with AERONET and is highly correlated with MODIS (Torres et al., 2007), with a correlation of 0.66 over land and 0.79 over the oceans (Curier et al., 2008). Due to the wavelength difference, the  $\tau$  measured by OMI at 442 nm has to be transferred to 550 nm using the Ångström exponent taken from AERONET at the time when OMI flies over the selected site. The  $\tau$  retrieved from AERONET also has to be converted to 550 nm to make them comparable.

### 3.1.3 AERONET micro-physical parameters

AERONET is an aerosol monitoring network of ground-based sun photometers. With standardized instruments, calibration, processing and distribution, AERONET provides a long-term global database for aerosol research and air-borne and space-borne measurement validation. The  $r_g$ ,  $P(\Theta)$  (Nakajima et al., 1983; Nakajima et al., 1996),  $\omega_0$  (Dubovik et al., 1998),  $n_r$  and  $n_i$  (Dubovik and King, 2000) used as inputs for radiative transfer calculation are derived from multiple-angular measurement of sky radiance.

The nearest AERONET site to the fire sources of 2017 Chile wildfires is the Santiago Beauchef (33.46°S, 70.66°W). The dataset in use is version 2 level 1.5 inversion product. To minimize the influence of temporal difference, the micro-physical parameters of AERONET measured near the time when OMI was flying over the site are used to simulate the optical properties of Mie scattering aerosols in DISAMAR. It is notable that the level 1.5 dataset is not quality-assured, and the location of this site is in downtown of Santiago City and close to major roads. These facts may bias the measurements.

The AERONET measurements need to be processed into the inputs required by DISAMAR. Firstly, a conversion from the volume size distribution  $V(r_v, \sigma_v)$  provided by AERONET to the number size distribution  $N(r_g, \sigma_g)$  used in DISAMAR is required:

$$N(r_g, \sigma_g) = V(r_v, \sigma_v) \frac{3}{4\pi r_g^3} e^{-4.5\sigma_g^2}, \quad (4)$$

The following relation between the geometric and volumetric mean radii ( $r_g$  and  $r_v$ ) and standard deviations ( $\sigma_g$  and  $\sigma_v$ ) is assumed:

$$r_g = r_v e^{-3\sigma_g^2}, \quad (5)$$

$$\sigma_g = \sigma_v, \quad (6)$$

The fine and coarse mode are derived separately from AERONET, and the optical properties of bi-modal aerosols in DISAMAR are calculated by externally mixing the derived modes with a fraction:

$$w_f = \frac{N_f(r_{g,f}, \sigma_{g,f})}{N_f(r_{g,f}, \sigma_{g,f}) + N_c(r_{g,c}, \sigma_{g,c})}, \quad (7)$$

$$w_c = 1 - w_f, \quad (8)$$

Then the weights for calculating the total  $\omega_0$  of the mixed aerosol are:

$$w_{\sigma,f} = \frac{w_f \sigma_f}{w_f \sigma_f + w_c \sigma_c}, \quad (9)$$

$$w_{\sigma,c} = 1 - w_{\sigma,f}, \quad (10)$$

Where the  $\sigma_f$  and  $\sigma_c$  are the extinction cross section of the fine and coarse aerosols. The expansion coefficients of the mixed aerosol is weighed by the  $\omega_0$  of the fine and coarse aerosols ( $\omega_{0,f}$  and  $\omega_{0,c}$ ), respectively:

$$w_{\omega_0,f} = \frac{w_f \sigma_f \omega_{0,f}}{w_f \sigma_f \omega_{0,f} + w_c \sigma_c \omega_{0,c}}, \quad (11)$$



$$w_{\omega_0,c} = 1 - w_{\omega_0,f}, \quad (12)$$

Secondly, the measuring wavelength of the AERONET instrument at this site only covers the visible band. To constrain the spectral dependency of optical properties in the near-UV band, complex refractive index  $n_r$  and  $n_i$  are linearly extrapolated using available data between 440 and 675 nm. Finally, the AERONET retrieved  $\omega_0$  is also linearly interpolated at 550 nm due to discrete sampling bands.

### 3.1.4 CALIOP backscattering coefficient

The CALIOP on-board CALIPSO launched in 2006 provides high-resolution profiles of aerosols and clouds. It has three channels with one measuring the backscattering intensity at 1064 nm and the rest measuring orthogonally polarized components at 532 nm backscattering intensity (Winker and Omar, 2006). Due to the limited spatial coverage, CALIOP did not observe the plume for all the cases for which we have OMI observations. In this study, we use the total attenuated backscatter at 532 nm from level 1B Version 4.10 Standard data to evaluate the parameterized aerosol profiles.

## 3.2 Methodology

In this study, we employ the radiative transfer model DISAMAR to simulate the near-UV AAI from OMI and to derive the  $\omega_0$  for a specific case, i.e. the Chile wildfires in January 2017. We select the period from 26 to 30 January 2017 (28 January is excluded due to lack of data) when the AAI value reached its peak. Except for the measurement geometry and surface conditions, the aerosol inputs used in the radiative transfer calculation should be independent of OMI measurements. The aerosol information consists of the cloud free column  $\tau$  retrieved from MODIS, and the aerosol micro-physical parameters ( $r_g$ ,  $n_r$  and  $n_i$ ) retrieved from AERONET.

The observed aerosol vertical information is limited for the Chile wildfires. Instead, we implement the same parameterization as in the sensitivity study to obtain the aerosol profile. Since the AAI dependency on  $\Delta z$  is minor (Fig.4 (c)), and to reduce the computational cost,  $\Delta z$  is set constant of 2 km based on the information from the CALIOP measurements of backscattering coefficient ( $\beta$ ) at 532 nm (Fig.7). The  $z_{\text{aer}}$ , to which the AAI is highly sensitive, is treated as a variable to be retrieved together with  $\omega_0$ .

With various combinations of  $z_{\text{aer}}$  and  $\omega_0$ , a lookup table (LUT) of the calculated AAI is constructed with DISAMAR. It should be noted that for all ground pixels in the plume we assume the same aerosol microphysical properties as well as the same vertical profile. Pixels outside the plume may have had significantly different properties and this will affect the results. Besides, the data size of the pre-processed OMI measurements is relatively small and the sample distribution is rather sparse, which implies that the dataset is quite sensitive to outliers.

Consequently, we apply a data quality control procedure. First, we manually remove the pixels that are geographically isolated from the main plume. Furthermore, we filter the dataset using an outlier detection based on the interquartile range (IQR) of the AAI difference between DISAMAR simulations and OMI measurements. According to Tukey's fences (Tukey, 1977), an AAI difference falling outside range between  $Q1-1.5 \text{ IQR}$  and  $Q3+1.5 \text{ IQR}$  may be regarded as an outlier and removed, where  $Q1$  and  $Q3$  are the first and third quartiles of the AAI difference, and the IQR is the range between  $Q1$  and  $Q3$ . Only the data passing the outlier detection criterion is used to calculate the cost function (Eq.(3)):

$$\text{RMSE} = \sqrt{\frac{\sum_i^n (AAI_{DSM,i}^{\text{qualified}} - AAI_{OMI,i})^2}{n}}, \quad (3)$$

Here  $AAI_i$  indicates the AAI for  $i$ th ground pixel of the selected OMI data; subscripts  $DSM$  and  $OMI$  indicate DISAMAR simulation and OMI observation, respectively. The combination of  $z_{\text{aer}}$  and  $\omega_0$  that leads to the minimum residue is used to simulate the AAI.



Finally, the simulated AAI is compared with OMI observations. We also employ the independent data from GOME-2 on  
275 MetOp-A/B as a reference to evaluate the potential bias of OMI. Similarly, the  $\tau$  retrieved from OMI and AERONET serves  
as a reference to that of MODIS. The estimated aerosol profile and  $\omega_0$  at 550 nm are evaluated with independent  
observations from CALIOP and AERONET, respectively.

#### 4 Results

In this study, we quantitatively retrieved the aerosol profile and  $\omega_0$  of the Chile 2017 wildfires by AAI simulation. The OMI  
280 measurements of the plume are displayed in Fig.8 (a) – (d). The presented ground pixels are with AAI value larger than 1  
and are free from the cloud contamination, the sun-glint effect over the ocean or the row anomaly of the instrument.  
Fortunately, the remaining data is still able to capture the plume features. It can be clearly seen that from 26 to 30 January,  
the plume produced by wildfires in the central Chile was transported by the south-easterly trade wind from the continent  
towards the lower latitude region of the Pacific Ocean. The plume travelled over 3000 km during the period.

285 The vertical movement of the plume is given by CALIOP backscattering coefficient measurements ( $\beta$ ) at 532 nm (Fig.7).  
The CALIOP paths closest to the plume are marked by a black dashed line in Fig.7. But it is noted that CALIOP probably  
did not always measure the plume feature, and may even fail to capture the elevated plume, e.g. on 26 January. The aerosol  
layer captured by CALIOP is distributed from 2 km to 6 km, with an average height at approximately 4-5 km. The ascending  
plume was driven by the heat generated by the fires and sunlight absorption, as well as the atmospheric vertical motions.

290 Fig.8 (e) – (h) show the AAI simulation selected by the data quality control mentioned in Section 3.2. The spatial  
distribution of the simulated AAI shows similar patterns as the OMI observations. Some data points that are geographically  
isolated from the plume, e.g. in case 26 and 30 January, differ strongly from what are observed inside the plume. Including  
these outliers in the optimization could bias the retrieved aerosol properties. This can also be seen in Fig.8 (i) – (l), where the  
points passing the data quality control described in Section 3.2 are highlighted in red colour. By removing the outliers, the  
295 average spatial correlation coefficient reaches 0.90.

Table 2 lists the statistics of the qualified AAI data, in terms of the median, relative difference and RMSE. The median of  
measured AAI ranges from 2 to 4 during the research period. Except for 26 January, the median of simulated AAI is in good  
agreement with the measurements, with relative differences within  $\pm 6\%$ . The low RMSE confirms the high spatial  
consistency between simulation and observation. The majority of the simulated AAI of 26 January is negatively biased,  
300 which is reflected by the small slope without an intercept correction in Fig.8 (i). A systematic bias in the inputs might cause  
this result.

In terms of  $\omega_0$ , both the AERONET measured and the AAI retrieved aerosol absorption become weaker with time (Table 2),  
which reflects the smoke ageing process (Reid et al., 2004). The mean of the retrieved  $\omega_0$  at 550 nm is 0.84, while the  
AERONET measurements provide mean value of 0.90. This might be due to the fact that the selected AERONET site is not  
305 exactly at the primary biomass burning regions as mentioned in section 3.1.3. The  $\omega_0$  measured by AERONET could  
increase as the result of aerosol ageing. Specifically, the location of the AERONET site is in the downtown, where the more  
reflective urban or industrial aerosols may mix with the smoke and enhance the measured  $\omega_0$ . Besides, it is also reported that  
AERONET tends to underestimate the absorption of biomass burning aerosols compared with in situ measurements  
(Dubovik et al., 2002; Reid et al., 2004). Last but not least, the micro-physics parameters retrieved from AERONET are not  
310 error-free. The uncertainty of size distribution retrieval is minor for biomass burning aerosols (Dubovik et al., 2000). Under  
optically thick circumstances when retrievals are quality-assured, the reported accuracy of complex refractive index is 0.04  
for  $n_r$  and 30%-50% for  $n_i$ , respectively (Dubovik et al., 2002). For biomass burning aerosols particularly, the uncertainty of  
 $\omega_0$  is 0.03 under high aerosol loading while only 0.05-0.07 under low aerosol loading (Dubovik et al., 2002; Holben et al.,  
2006).



315 Although AERONET could overestimate the  $\omega_0$ , information from other datasets could also bias the aerosol absorption. Among all the inputs, the parameterization of a one-layer box-shape aerosol profile could be the largest error source due to the lack of observations. Although the influence of  $\Delta z$  on the AAI is small (Fig.4 (c)), the AAI calculation highly depends on  $z_{\text{aer}}$  (Fig.4 (b)). As shown in Table 2, the estimated plume altitude varies from 4.5 to 4.9 km. As the black solid line indicated in Fig.7, the retrieved  $z_{\text{aer}}$  can accurately capture the measured geometric vertical location of the plume. The  $z_{\text{aer}}$  on 26  
320 January seems overestimated because of the temporal and spatial difference. Concretely, CALIOP sampled the plume near the sources and close to the surface, while the plume observed by OMI had been already elevated and transported to the open ocean. The lack of information on the real plume height makes it challenging to determine the main reason responsible for the systematic bias in Fig.8 (i). Except for 26 January,  $z_{\text{aer}}$  is in good agreement with what CALIOP observed. One should keep in mind that although the retrieved aerosol profiles are convincing to some extent, CALIOP and OMI observations are  
325 not exactly co-located. Besides, the retrieved aerosol profile may fail to represent the spatial variation of the plume. The uncertainty cannot be directly determined due to the lack of validation observations.

However, even with relative reasonable retrieval of  $z_{\text{aer}}$ , it is noted that the  $\omega_0$  retrieved on 27 January is significantly underestimated and biased from the mean level of other cases. This implies the existence of other error sources, such as the observational errors from the input  $\tau$  of MODIS and the AAI of OMI to be fit. We investigate the potential bias of these two  
330 datasets by plotting the histogram of the AAI measurement difference between GOME-2 and OMI (Fig.9 (a)), against the  $\tau$  measurement difference between MODIS and OMI (Fig.9 (b)). It is clear that on 27 January, the AAI from OMI seems to be overestimated, while the  $\tau$  from MODIS could be potentially underestimated. Fitting a higher AAI with a lower input  $\tau$  leads to an overestimation in aerosol absorption. But one should keep in mind that the difference in wavelength pair choice for AAI retrieval, measurement time and condition, etc. could also be responsible for the AAI discrepancy between GOME-2  
335 and OMI. Exploring the difference between the two datasets is beyond the scope of this study. Hereby we quantify the impact of  $\tau$  for this specific case by systematically enhancing the  $\tau$  of MODIS with a constant variation ( $\Delta\tau$ ) added to all sample points, with the AAI level and the aerosol profile remain unchanged. Fig.9 (c) presents how the estimated AAI RMSE and  $\omega_0$  respond to the enhanced  $\tau$ . It can be clearly seen that an increase in overall  $\tau$  level by 0.07 raises  $\omega_0$  to 0.84, and optimizes the AAI simulation to a RMSE less than 0.45. If we apply this  $\tau$  adaption, the retrieved  $\omega_0$  of 27 January will  
340 be more consistent with other cases.

Apart from the observational errors in AERONET, OMI and MODIS data, the assumption that the plume features are homogeneous and static plume could also result in the discrepancy between AAI retrieved and AERONET measured  $\omega_0$ . In reality, the plume altitude, the optical properties and even the chemical compositions could vary in space and time, while our simulations neglect those effects.

## 345 5 Conclusions

Biomass burning is a major source of absorbing aerosols such as BC, posing a significant contribution on climate warming. Quantitatively characterizing the absorption by biomass burning aerosols is therefore important to reduce the uncertainty in assessments of global radiative forcing. Facing the lack of long-term  $\omega_0$  records, this study provides an approach to retrieve  $\omega_0$  based on reflectivity in the near-UV channel measured by OMI. Although AAI is not a geophysical parameter and  
350 depends on many parameters, its independence from pre-defined aerosol types, its high sensitivity to aerosol absorption as well as its long data record, makes it an attractive parameter for climate studies.

We test the retrieval of  $\omega_0$  for the wildfires happening in central Chile in January 2017. After filtering the data for outliers, the high spatial correlation coefficients (over 0.85) between the simulated and observed AAI proves its usefulness and effectiveness. The retrieved aerosol profiles indicate the plume was elevated to height of 4.5-4.9 km during the research  
355 period. These results are in agreement with CALIOP measurements. This retrieved  $\omega_0$  at 550 nm of the Chile wildfires plume



is approximately 0.84, which is 0.06 lower than that of AERONET retrieval. The retrieved  $\omega_0$  is reasonable, taking into account the typical uncertainty in the  $\omega_0$  retrieved from AERONET ( $\pm 0.03$ ). The remaining discrepancy is probably caused by: the location of the AERONET site outside the range of the plume; the assumption of homogeneous and static plume properties, which ignores the plume evolution over space and time; the simplified parameterization of the aerosol profile; and the observational errors in AAI and  $\tau$ , as well as the aerosol micro-physics. We quantitatively analyse the uncertainty of  $\tau$  for a specific case (27 January) when the estimated aerosol profile is in good agreement with the CALIOP measurements. This study proves the potential of utilizing OMI measured AAI to quantitatively characterize aerosol optical properties like  $\omega_0$ . Even without direct observation of aerosol profiles, this parameter can also be retrieved with quite good confidence. However, apart from the observational uncertainties, the current study is probably somewhat limited by the necessary assumptions of homogeneous and static plume properties, whose impact on retrieved  $\omega_0$  is difficult to quantify. In the future planned work, a chemistry transport model is needed to describe the evolution of the plume properties in space and time. Moreover, also clouds should be taken into consideration in order to use the AAI observations over clouds, thus making the maximum use of the near-UV observations.

#### Acknowledgements

This work was performed in the framework of the KNMI Multi-Annual Strategic Research (MSO).

#### References

- Adler, G., Flores, J. M., Abo Riziq, A., Borrmann, S. and Rudich, Y.: Chemical, physical, and optical evolution of biomass burning aerosols: A case study, *Atmos. Chem. Phys.*, 11, 1491–1503, doi:10.5194/acp-11-1491-2011, 2011.
- Bäumer, D., Vogel, B., Versick, S., Rinke, R., Möhler, O. and Schnaiter, M.: Relationship of visibility, aerosol optical thickness and aerosol size distribution in an ageing air mass over South-West Germany, *Atmos. Environ.*, 42, 989–998, doi:10.1016/j.atmosenv.2007.10.017, 2008.
- Bond, T. C., Streets, D. G., Yarber, K. F., Nelson, S. M., Woo, J. H. and Klimont, Z.: A technology-based global inventory of black and organic carbon emissions from combustion, *J. Geophys. Res. D Atmos.*, 109, D14203, doi:10.1029/2003JD003697, 2004.
- Bond, T. C., Doherty, S. J., Fahey, D. W., Forster, P. M., Berntsen, T., Deangelo, B. J., Flanner, M. G., Ghan, S., Kyrcher, B., Koch, D., Kinne, S., Kondo, Y., Quinn, P. K., Sarofim, M. C., Schultz, M. G., Schulz, M., Venkataraman, C., Zhang, H., Zhang, S., Bellouin, N., Guttikunda, S. K., Hopke, P. K., Jacobson, M. Z., Kaiser, J. W., Klimont, Z., Lohmann, U., Schwarz, J. P., Shindell, D., Storelvmo, T., Warren, S. G. and Zender, C. S.: Bounding the role of black carbon in the climate system: A scientific assessment, *J. Geophys. Res. Atmos.*, 118, 5380–5552, doi:10.1002/jgrd.50171, 2013.
- Buchard, V., Silva, A. M., Colarco, P. R., Darmenov, A., Randles, C. A., Govindaraju, R., Torres, O. and Goddard, N.: Using the OMI aerosol index and absorption aerosol optical depth to evaluate the NASA MERRA Aerosol Reanalysis, *Atmos. Chem. Phys.*, 15, 5743–5760, doi:10.5194/acp-15-5743-2015, 2015.
- Corr, C. A., Krotkov, N., Madronich, S., Slusser, J. R., Holben, B., Gao, W., Flynn, J., Lefer, B., Kreidenweis, S. M., Collins, F., Sciences, E., County, B., Division, A. C., Resource, N., Collins, F., Branch, B. S. and Sciences, A.: Retrieval of aerosol single scattering albedo at ultraviolet wavelengths at the T1 site during MILAGRO, *Atmos. Chem. Phys.*, 9, 5813–5827, 2009.
- Curier, R. L., Veefkind, J. P., Braak, R., Veihelmann, B., Torres, O. and de Leeuw, G.: Retrieval of aerosol optical properties from OMI radiances using a multiwavelength algorithm: Application to western Europe, *J. Geophys. Res. Atmos.*, 113, D17S90, doi:10.1029/2007JD008738, 2008.
- Deroubaix, A., Martiny, N., Chiapello, I. and Marticorena, B.: Remote Sensing of Environment Suitability of OMI aerosol



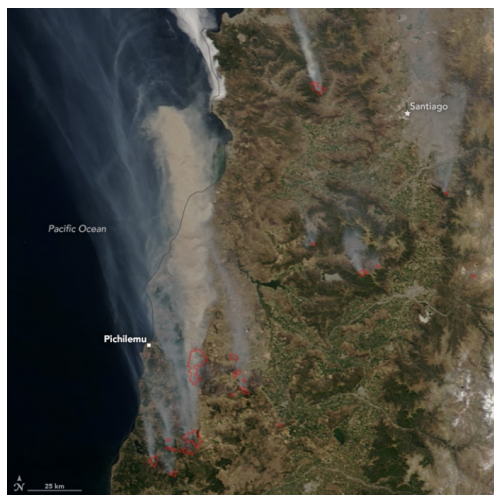
- index to reflect mineral dust surface conditions: Preliminary application for studying the link with meningitis epidemics in the Sahel, *Remote Sens. Environ.*, 133, 116–127, doi:10.1016/j.rse.2013.02.009, 2013.
- de Graaf, M., Stammes, P., Torres, O. and Koelemeijer, R. B. A.: Absorbing Aerosol Index: Sensitivity analysis, application to GOME and comparison with TOMS, *J. Geophys. Res. D Atmos.*, 110, D01201, doi:10.1029/2004JD005178, 2005.
- 400 de Haan, J. F.: DISAMAR Algorithm description and background information, De Bilt, 2011.
- de Haan, Johan F., Bosma, P.B and Hovenier, J. W.: The adding method for multiple scattering of polarized light, *Astron. Astrophys.*, 183, 371–391, 1987.
- Dubovik, O., Holben, B., Eck, T. F., Smirnov, A., Kaufman, Y. J., King, M. D., Tanré, D., Slutsker, I., Sciences, G. E. and Directorate, E. S.: Variability of Absorption and Optical Properties of Key Aerosol Types Observed in Worldwide  
405 Locations, *J. Atmos. Sci.*, 59(3), 590–608, doi:10.1175/1520-0469(2002)059<0590:VOAAOP>2.0.CO;2, 2002.
- Dubovik, O., Holben, B. N., Kaufman, Y. J., Yamasoe, M., Smirnov, A., Tanré, D. and Slutsker, I.: Single-scattering albedo of smoke retrieved from the sky radiance and solar transmittance measured from ground, *J. Geophys. Res.*, 103, 31903–31923, doi:10.1029/98JD02276, 1998.
- Dubovik, O. and King, M. D.: A flexible inversion algorithm for retrieval of aerosol optical properties from Sun and sky  
410 radiance measurements, *J. Geophys. Res.*, 105, 20637–20969, doi:10.1029/2000JD900282, 2000.
- Dubovik, O., Smirnov, A., Holben, B. N., King, M. D., Kaufman, Y. J., Eck, T. F. and Slutsker, I.: Accuracy assessments of aerosol optical properties retrieved from Aerosol Robotic Network (AERONET) Sun and sky radiance measurements, *J. Geophys. Res.*, 105, 9791–9806, doi:10.1029/2000JD900040, 2000.
- Eck, T. F., Holben, B. N., Reid, J. S., Mukelabai, M. M., Piketh, S. J., Torres, O., Jethva, H. T., Hyer, E. J., Ward, D. E.,  
415 Dubovik, O., Sinyuk, A., Schafer, J. S., Giles, D. M., Sorokin, M., Smirnov, A. and Slutsker, I.: A seasonal trend of single scattering albedo in southern African biomass-burning particles: Implications for satellite products and estimates of emissions for the world's largest biomass-burning source, *J. Geophys. Res.*, 118, 6414–6432, doi:10.1002/jgrd.50500, 2013.
- Eck, T. F., Holben, B. N., Ward, D. E., Mukelabai, M. M., Dubovik, O., Smirnov, A., Schafer, J. S., Hsu, N. C., Piketh, S. J.,  
420 Queface, A., Roux, J. Le, Swap, R. J. and Slutsker, I.: Variability of biomass burning aerosol optical characteristics in southern Africa during the SAFARI 2000 dry season campaign and a comparison of single scattering albedo estimates from radiometric measurements, *J. Geophys. Res.*, 108, 8477, doi:10.1029/2002JD002321, 2003.
- Ginoux, P., Prospero, J. M., Torres, O. and Chin, M.: Long-term simulation of global dust distribution with the GOCART model: Correlation with North Atlantic Oscillation, *Environ. Model. Softw.*, 19, 113–128, doi:10.1016/S1364-  
425 8152(03)00114-2, 2004.
- Ginoux, P. and Torres, O.: Empirical TOMS index for dust aerosol: Applications to model validation and source characterization, *J. Geophys. Res.*, 108, 4534, doi:10.1029/2003JD003470, 2003.
- Herman, J. R., Bhartia, P. K., Torres, O., Hsu, C., Sefter, C. and Celarier, E.: Global distribution of UV-absorbing aerosols from Nimbus 7/TOMS data, *J. Geophys. Res.*, 102, 16911–16992, doi:10.1029/96JD03680, 1997.
- 430 Holben, B. N., Eck, T. F., Slutsker, I., Smirnov, A., Sinyuk, A., Schafer, J., Giles, D., Dubovik, O. and Lille, U. S. T. De: AERONET's Version 2.0 quality assurance criteria, *Int. Soc. Opt. Photonics*, 6408, 64080Q, 2006.
- Hsu, N. C., Tsay, S. C., King, M. D. and Herman, J. R.: Aerosol properties over bright-reflecting source regions, *IEEE Trans. Geosci. Remote Sens.*, 42, 557–569, doi:10.1109/TGRS.2004.824067, 2004.
- Hu, R. M., Martin, R. V. and Fairlie, T. D.: Global retrieval of columnar aerosol single scattering albedo from space-based  
435 observations, *J. Geophys. Res. Atmos.*, 112, D02204, doi:10.1029/2005JD006832, 2007.
- Ialongo, I., Buchard, V., Brogniez, C., Casale, G. R. and Siani, A. M.: Aerosol Single Scattering Albedo retrieval in the UV range: an application to OMI satellite validation, *Atmos. Chem. Phys.*, 10, 331–340, 2010.



- IPCC, 2007: Climate Change 2007: Synthesis Report. Contribution of Working Groups I, II and III to the Fourth Assessment Report of the Intergovernmental Panel on Climate Change [Core Writing Team, Pachauri, R.K and Reisinger, A. (eds.)].  
440 IPCC, Geneva, Switzerland, 104 pp.
- IPCC, 2014: Climate Change 2014: Synthesis Report. Contribution of Working Groups I, II and III to the Fifth Assessment Report of the Intergovernmental Panel on Climate Change [Core Writing Team, R.K. Pachauri and L.A. Meyer (eds.)].  
IPCC, Geneva, Switzerland, 151 pp.
- Kaskaoutis, D.G.; Nastos, P.T.; Kosmopoulos, P.G.; Kambezidis, H.D.; Kharol, S.K. and Badarinath, K. V. S.: The Aura –  
445 OMI Aerosol Index distribution over Greece, Atmos. Res. J., 98, 28–39, doi:10.1016/j.atmosres.2010.03.018, 2010.
- Kassianov, E. I., Barnard, J. C. and Ackerman, T. P.: Retrieval of aerosol microphysical properties using surface MultiFilter Rotating Shadowband Radiometer (MFRSR) data: Modeling and observations, J. Geophys. Res., 110, D09201, doi:10.1029/2004JD005337, 2005.
- Kaufman, Y. J.: Aerosol Optical Thickness and Atmospheric Path Radiance, J. Geophys. Res., 98, 2677–2692,  
450 doi:10.1029/92JD02427, 1993.
- Kaufman, Y. J., Tanré, D., Remer, L. A., Vermote, E. F., Chu, A. and Holben, B. N.: Operational remote sensing of tropospheric aerosol over land from EOS moderate resolution imaging spectroradiometer, J. Geophys. Res., 102, 17051–17067, doi:10.1029/96JD03988, 1997.
- Kaufman, Y. J., Tanré, D. and Boucher, O.: A Satellite View of Aerosols in the Climate System, Nature, 419, 215–223,  
455 2002.
- Koch, D. and Del Genio, A. D.: Black carbon semi-direct effects on cloud cover: Review and synthesis, Atmos. Chem. Phys., 10, 7685–7696, doi:10.5194/acp-10-7685-2010, 2010.
- Lee, K. H., Li, Z., Wong, M. S., Xin, J., Wang, Y., Hao, W. and Zhao, F.: Aerosol single scattering albedo estimated across China from a combination of ground and satellite measurements, J. Geophys. Res., 112, D22S15,  
460 doi:10.1029/2007JD009077, 2007.
- Lee, K. H., Li, Z., Kim, Y. J. and Kokhanovsky, A.: Atmospheric Aerosol Monitoring from Satellite Observations: A History of Three Decades, in Atmospheric and Biological Environmental Monitoring, pp. 13–38., 2009.
- Leroy, M., Deuzé, J. L., Bréon, F. M., Hautecoeur, O., Herman, M., Buriez, J. C., Tanré, D., Bouffiès, S., Chazette, P. and Roujean, J. L.: Retrieval of atmospheric properties and surface bidirectional reflectances over land from POLDER/ADEOS,  
465 J. Geophys. Res., 102, 17023–17037, doi:10.1029/96JD02662, 1997.
- Levelt, P. F., Oord, G. H. J. Van Den, Dobber, M. R., Mälkki, A., Visser, H., Vries, J. De, Stammes, P., Lundell, J. O. V and Saari, H.: The Ozone Monitoring Instrument, IEEE Trans. Geosci. Remote Sens., 44, 1093–1101, 2006.
- Myhre, G., Shindell, D., Bréon, F. M., Collins, W., Fuglestedt, J., Huang, J., ... & Nakajima, T.: Anthropogenic and Natural Radiative Forcing, Clim. Chang., 432, 658–740, 2013.
- 470 Nakajima, T., Tanaka, M. and Yamauchi, T.: Retrieval of the optical properties of aerosols from aureole and extinction data, Appl. Opt., 22, 2951–2959, 1983.
- Nakajima, T., Tonna, G., Rao, R., Boi, P., Kaufman, Y. and Holben, B.: Use of sky brightness measurements from ground for remote sensing of particulate polydispersions, Appl. Opt., 35, 2672–2686, doi:10.1364/AO.35.002672, 1996.
- NASA.gov: NASA's Terra Catches Fires in Central Chile, [online] Available from: <https://www.nasa.gov/image-feature/goddard/2017/nasas-terra-catches-fires-in-central-chile> (Accessed 1 May 2017), 2017.
- Petters, J. L., Saxena, V. K., Slusser, J. R., Wenny, B. N. and Madronich, S.: Aerosol single scattering albedo retrieved from measurements of surface UV irradiance and a radiative transfer model, J. Geophys. Res., 108, 4288, doi:10.1029/2002JD002360, 2003.
- Ramanathan, V. and Carmichael, G.: Global and regional climate changes due to black carbon, Nat. Geosci., 1, 221–227,  
480 doi:10.1038/ngeo156, 2008.



- Reid, J. S., Eck, T. F., Christopher, S. A., Koppmann, R., Dubovik, O., Eleuterio, D. P., Holben, B. N., Reid, E. A. and Zhang, J.: A review of biomass burning emissions part III: intensive optical properties of biomass burning particles, *Atmos. Chem. Phys. Discuss.*, doi:10.5194/acpd-4-5201-2004, 2004.
- 485 Remer, L.A., Kaufman, Y.J., Tanré, D., Mattoo, S., Chu, D.A., Martins, J.V., Li, R.R., Ichiku, C., Levy, R.C., Kleidman, R.G., Eck, T.K., Vermote, E. and Holben, B. N.: The MODIS Aerosol Algorithm, Products, and Validation, *J. Atmos. Sci.*, 62, 947–973, 2005.
- Remer, L.A., Tanré, D. and Kaufman, Y. J.: Algorithm for remote sensing of tropospheric aerosol from MODIS:Collection 5 Product ID: MOD04/MYD04-C005., 1998.
- D.C. Stein Zweers: TROPOMI ATBD of the UV aerosol index., 2016.
- 490 Tanr, D., J Kaufman, B. Y., Herman, M. and Mattoo, S.: Remote sensing of aerosol properties over oceans using the MODIS/EOS spectral radiances, *J. Geophys. Res.*, 102, 16971–16988, doi:10.1029/96JD03437, 1997.
- The Guardian: Chile battles devastating wildfires: 'We have never seen anything on this scale', [online] Available from: [https://www.theguardian.com/world/2017/jan/25/chile-fire-firefighting-international-help?utm\\_source=Climate+News+Network&utm\\_campaign=afdf3cf10c-](https://www.theguardian.com/world/2017/jan/25/chile-fire-firefighting-international-help?utm_source=Climate+News+Network&utm_campaign=afdf3cf10c-EMAIL_CAMPAIGN_2017_02_03&utm_medium=email&utm_term=0_1198ea8936-afdf3cf10c-38798061)
- 495 EMAIL\_CAMPAIGN\_2017\_02\_03&utm\_medium=email&utm\_term=0\_1198ea8936-afdf3cf10c-38798061 (Accessed 25 Jan 2017), 2017.
- Torres, O., Bhartia, P. K., Herman, J. R., Ahmad, Z. and Gleason, J.: Derivation of aerosol properties from satellite measurements of backscattered ultraviolet radiation: Theoretical basis, *J. Geophys. Res. Atmos.*, 103, 17099–17110, doi:10.1029/98JD00900, 1998.
- 500 Torres, O., Bhartia, P. K., Sinyuk, A., Welton, E. J. and Holben, B.: Total Ozone Mapping Spectrometer measurements of aerosol absorption from space: Comparison to SAFARI 2000 ground-based observations, *J. Geophys. Res. D Atmos.*, 110, D10S18, doi:10.1029/2004JD004611, 2005.
- Torres, O., Tanskanen, A., Veihelmann, B., Ahn, C., Braak, R., Bhartia, P. K., Veefkind, P. and Levelt, P.: Aerosols and surface UV products from Ozone Monitoring Instrument observations: An overview, *J. Geophys. Res.*, 112, D24S47, doi:10.1029/2007JD008809, 2007.
- 505 Torres, O., Jethva, H. and Bhartia, P. K.: Retrieval of Aerosol Optical Depth above Clouds from OMI Observations: Sensitivity Analysis and Case Studies, *J. Atmos. Sci.*, 69, 1037–1053, doi:10.1175/JAS-D-11-0130.1, 2012.
- Tukey, J.W.: *Exploratory data analysis*, Addison-Wesley Publishing Company, 1977.
- Winker, D. M., Vaughan, M. A., Omar, A., Hu, Y., Powell, K. A., Liu, Z.; Hunt, W.H.; Young, S. A.: Overview of the CALIPSO Mission and CALIOP Data Processing Algorithms, *Technol. J. Atmos. Ocean.*, 26, 2310–2323, doi:10.1175/2009JTECHA1281.1, 2009.
- 510 Yin, B., Min, Q. and Joseph, E.: Retrievals and uncertainty analysis of aerosol single scattering albedo from MFRSR measurements, *J. Quant. Spectrosc. Radiat. Transf.*, 150, 95–106, doi:10.1016/j.jqsrt.2014.08.012, 2015.



520 **Figure 1: Chile wildfires detected by Terra/MODIS on 20 January 2017 (Image source: NASA's Earth Observatory**  
**<https://earthobservatory.nasa.gov/IOTD/view.php?id=89496>).**

525

530

535

540

545

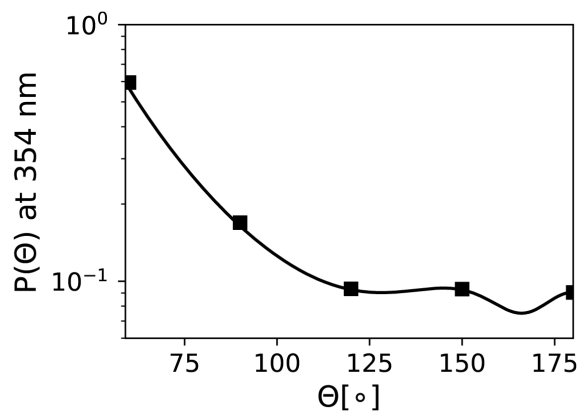


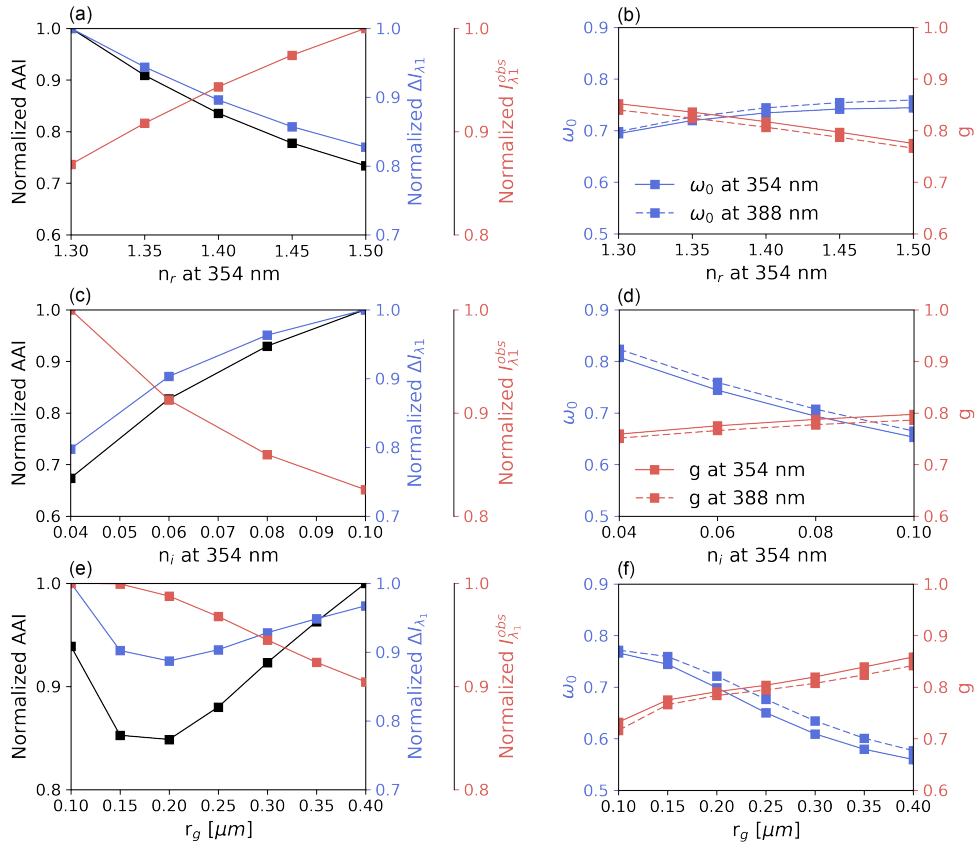
Figure 2: Phase function  $p(\Theta)$  at 354 nm of the parameterized Mie scattering aerosols in sensitivity analysis. The markers in the plot correspond to the value when  $\Theta=60^\circ, 90^\circ, 120^\circ, 150^\circ, 180^\circ$ .

550

555

560

565



570 **Figure 3:** AAI sensitivity to micro-physical parameters:  $n_i$  (a, b),  $n_r$  (c, d), and  $r_g$  (e, f). The left panels (a, c and e) show the sensitivity of the normalized AAI (black), the normalized  $\Delta I_{\lambda 1}$  (blue) and the normalized  $I_{\lambda 1}^{obs}$  (red). The right panels (b, d and f) show  $\omega_0$  (blue) and  $g$  (red) at wavelength 354 (solid line) and 388 (dashed line) nm, respectively.

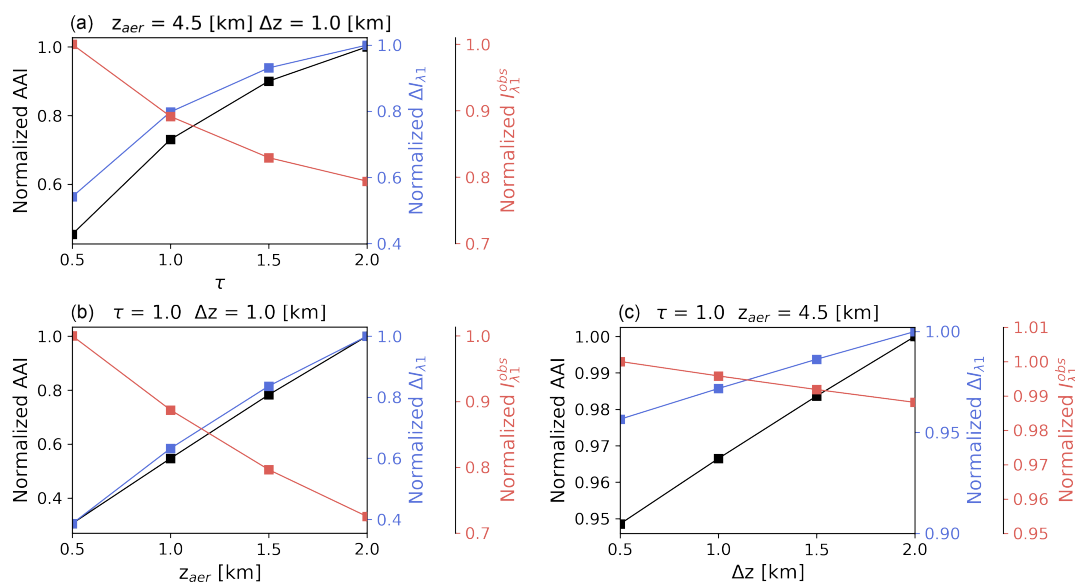


Figure 4: AAI sensitivity to macro-physical parameters: (a)  $\tau$  at 550 nm, (b)  $z_{aer}$  and (c)  $\Delta z$ .

575

580

585

590

595

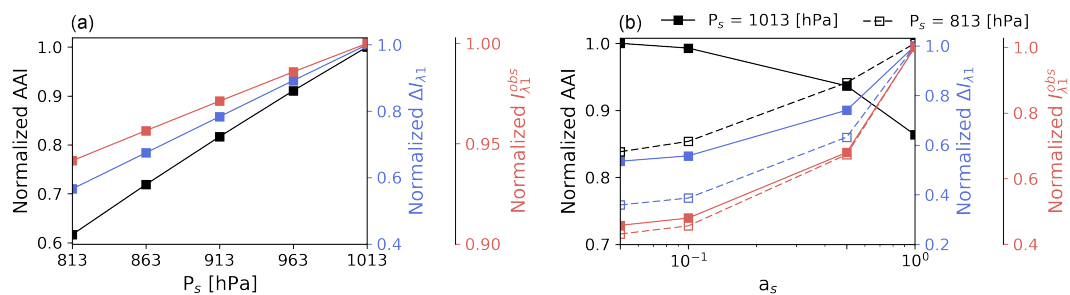


Figure 5 AAI sensitivity to surface parameters:  $a_s$ (a) and  $P_s$ (b). The solid line and dashed line in (b) indicates terrain height at sea level ( $P_s = 1013$  hPa) and elevated terrain height ( $P_s = 813$  hPa), respectively.

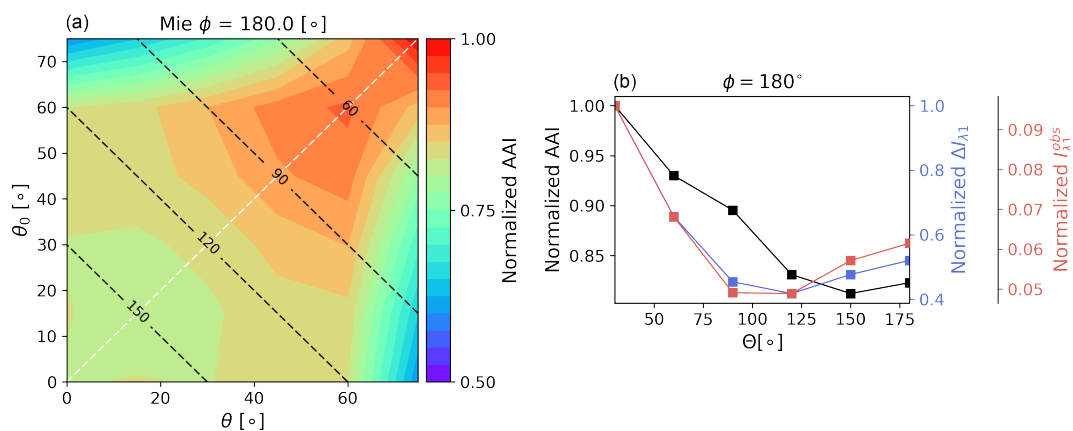
605

610

615

620

625



630 **Figure.6** AAI sensitivity to  $\theta$  and  $\theta_0$  at  $\phi=180^\circ$ . The black dashed contour in (a) indicates the  $\Theta=60^\circ, 90^\circ, 120^\circ, 150^\circ$ . The white  
 635 dashed line in (a) indicates the cross section.

635

640

645

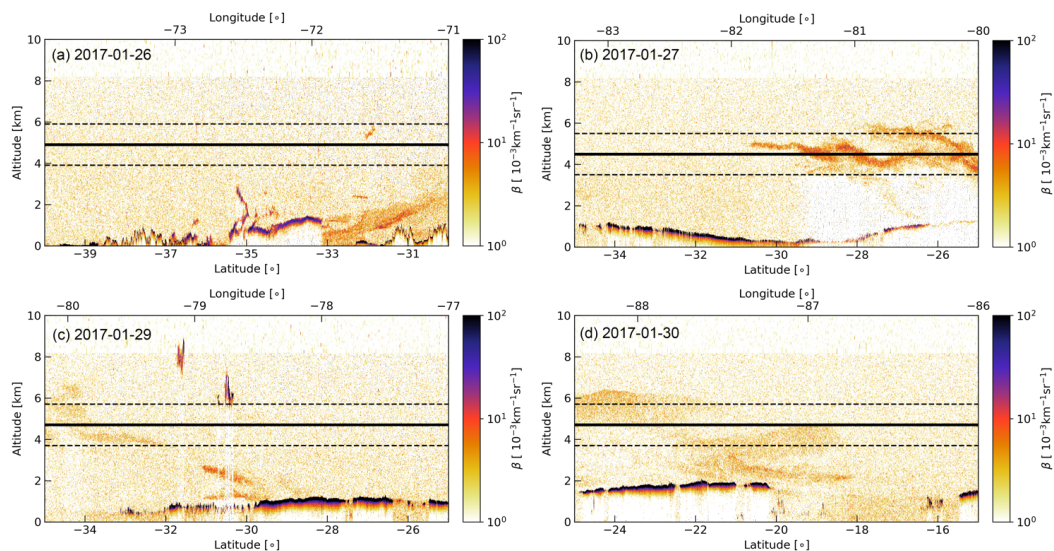
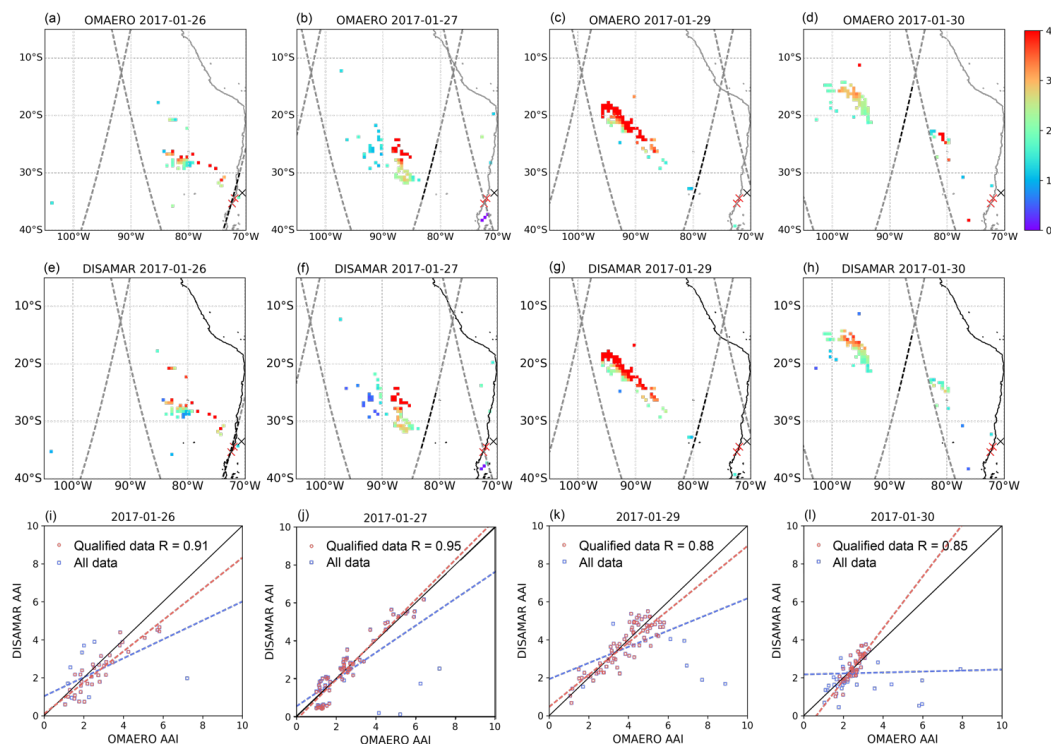


Figure.7 CALIOP backscatter coefficient  $\beta$  at 532 nm. The solid and dashed line indicate the retrieved  $z_{\text{aer}}$  and  $A_z$ , respectively.

650

655



660 **Figure.8** OMI observations (a–d) and DISAMAR simulations (e–h) of the Chile wildfires on 26, 27, 29 and 30 January 2017. The black and red cross symbols are the AERONET station and the main fire sources (Pichilemu W34.39° S72.00° and Constitución S35.33°, W72.42°), respectively. The grey dashed line indicates the CALIOP paths in the region of interest, where the paths used to validate the plume height are marked by black dashed line. The scatter plots (i–l) present the OMI observations against DISAMAR simulations for only qualified data (red dot) and all data (blue dot), respectively.

665

670

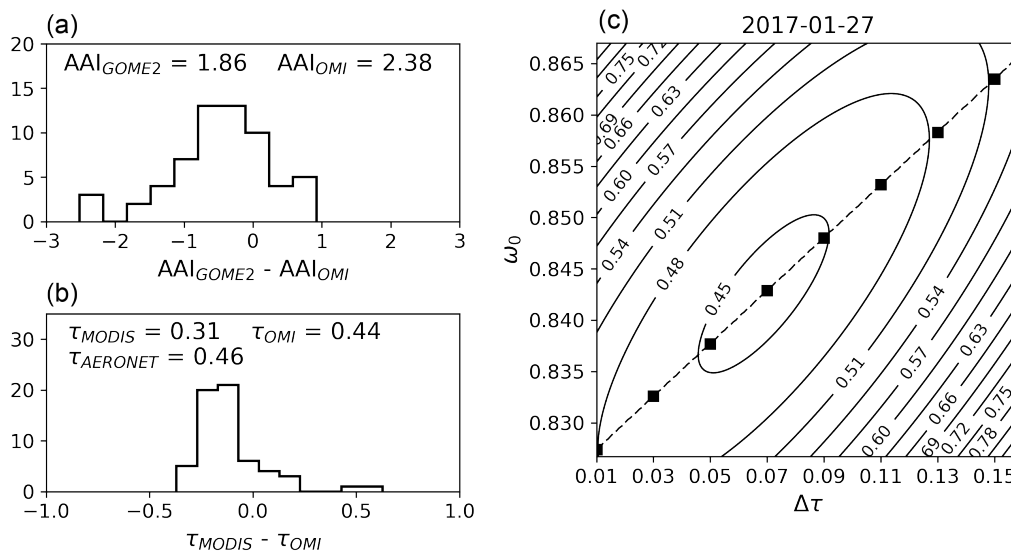


Figure.9 Histogram of (a) the AAI difference between GOME-2 and OMI, against (b) the  $\tau$  difference at 550 nm between MODIS and OMI for 27 January. Contour of (c) the AAI RMSE as a function of variation in  $\tau$  and  $\omega_0$  for 27 January. The dashed line is the best estimation for each pair of  $\Delta\tau$  and  $\omega_0$ .

675

680

685

690

695

**Table 1. Parameters used in sensitivity analysis.**

Parameters	Default value	Sensitivity range	Unit
Geometric mean radius ( $r_g$ )	0.15	0.1, 0.15, 0.2, 0.25, 0.3, 0.35, 0.4	$\mu\text{m}$
Geometric standard deviation ( $\sigma_g$ )	1.5	-	$\mu\text{m}$
Real refractive index ( $n_r$ ) at 354 nm	1.5	1.3, 1.35, 1.4, 1.45, 1.5	-
Imaginary refractive index ( $n_i$ ) at 354 nm	0.06	0.04, 0.06, 0.08, 0.1	-
Aerosol layer geometric central height ( $z_{\text{aer}}$ )	4.5	2.5, 4.5, 6.5, 8.5	km
Aerosol layer geometric thickness ( $\Delta z$ )	1	0.5, 1, 1.5, 2	km
Aerosol optical thickness ( $\tau$ ) at 550 nm	1	0.5, 1, 1.5, 2	-
Surface albedo ( $a_s$ )	0.05	0.05, 0.1, 0.5, 1.0	-
Surface pressure ( $P_s$ )	1013	1013, 963, 913, 863, 813	hPa
Solar zenith angle ( $\theta_0$ )	30	0, 15, 30, 45, 60, 75	$^\circ$
Viewing zenith angle ( $\theta$ )	0	0, 15, 30, 45, 60, 75	$^\circ$
Relative azimuth angle ( $\Delta\varphi = \varphi - \varphi_0 + 180^\circ$ )	0	0, $\pm 45$ , $\pm 90$ , $\pm 135$ , $\pm 180$	$^\circ$

700

705

710

715

720



**Table.2 Summary of simulation results (applying IQR outlier detection).**

Date		2017-01-26	2017-01-27	2017-01-29	2017-01-30
AAI	AAI median (OMAERO)	2.52	2.38	4.05	2.61
	AAI median (DISAMAR)	2.17	2.48	3.81	2.49
	Relative difference (%)	-13.88	4.20	-5.93	-4.60
	RMSE	0.67	0.51	0.60	0.41
Aerosol profile	$z_{\text{aer}}$ [km]	4.9	4.5	4.7	4.7
	$\Delta z$ [km]			2	
$\omega_0$ at 550 nm	$\omega_0$ (AERONET)	0.89	0.89	0.92	0.91
	$\omega_0$ (DISAMAR)	0.83	0.81	0.87	0.85
	Relative difference (%)	-6.74	-8.99	-5.43	-6.59